# HIGH RESOLUTION COMPUTATIONAL INVESTIGATION OF TRIMMED COAXIAL ROTOR AERODYNAMICS IN HOVER

Vinod K Lakshminarayan [*]
James D. Baeder [†]

Alfred Gessow Rotorcraft Center
Department of Aerospace Engineering
University of Maryland
College Park, MD 20742.

## Abstract

In this work, a compressible Reynolds Averaged Navier Stokes (RANS) solver is used to investigate the aerodynamics of a coaxial rotor configuration under hovering conditions; in order to evaluate the predictive capability of the computational approach and to characterize the unsteadiness in the aerodynamic flow field of a coaxial system. Compared to previous work by the authors, the present calculations use finer mesh along with smaller time step size, thereby aiding in a better capture and preservation of the wake. Additional benefits are attained from improvements in the sliding mesh boundary interpolation scheme. A trimming procedure is implemented, which allows for detailed yaw and thrust trim. The global quantities such as thrust and power are predicted reasonably well. In the torque trimmed situation, the top rotor shares significant percentage of the total thrust at lower thrust levels, which decreases to about 55% of the total thrust at higher thrust values. The interaction between the rotor systems is seen to generate significant impulses in the instantaneous thrust and power. The characteristic signature of this impulse is explained in terms of the blade thickness (a *venturi effect*) and loading (an *upwash-downwash* effect). Further, interaction of the top-rotor wake with the blades of the bottom rotor results in low-harmonic unsteadiness. The flow field of the coaxial system is very complicated due to various blade-vortex and vortex interactions. The wake of the top rotor contracts faster compared to that of the bottom rotor because of the vortex-vortex interaction. Further, the top rotor wake convects vertically down at a faster rate due to increased inflow.

## Introduction

Conceptually, the coaxial rotor configuration offers substantial design advantages over the conventional main rotor tail-rotor configuration. Perhaps most significantly, the additional power requirements and weight associated with the tail rotor, tail boom and transmission system may be reallocated for additional payload capability. Additionally, the asymmetry of lift associated with a single rotor in forward flight is mitigated, offering the potential for a faster and more stable vehicle. Reductions in size and noise are also advantages often cited for the conceptual coaxial configuration.

However, in a coaxial rotor configuration, the two rotors and their wakes interact with each other, producing a more complicated flow field than is found in a single rotor system. A major portion of the lower rotor continually operates in the wake system of the upper rotor. This has a significant effect on the inflow distribution of the overall system, and also on the boundary layer of the lower rotor blades. This interacting flow can, in general, result in a loss of net rotor system aerodynamic efficiency. Additionally, this can result in an undesired unsteadiness in the flow field even under hovering conditions.

Coleman (Ref. 1) presents a concise summary of coaxial rotor experiments along with a comprehensive list of relevant citations on performance, wake characteristics, and proposed methods of performance analysis. Traditionally, for multiple rotor systems, simple analyses such as blade element momentum theory (Refs. 2, 3) or vortex filament methods (VFM) (Refs. 2, 4–8) have been used. These methods can provide for a qualitative understanding of the phenomena and predict global performance characteristics within reasonable accuracy. Recently, the Vorticity Transport Model (VTM) (Ref. 9) has been applied to the coaxial rotor system. In this ap-

---

[*] Graduate Research Assistant, vinodkl@umd.edu

[†] Associate Professor, baeder@eng.umd.edu

Presented at the AHS International Specialists' Conference on Aeromechanics, San Francisco, CA, January 23–25, 2008.

proach, the wake vorticity is determined from a lifting line-based approach and is evolved in the flow-field using an Eulerian solution of the inviscid, incompressible vorticity transport equations. The representation of the wake is of a much higher quality, and as a result, more accurate performance predictions are reported. Though the aforementioned methods are efficient and are capable of producing accurate results, the following limitations have been observed:

- A certain degree of empiricism is involved. For instance, in VFM, initial core-radius and vortex roll-up are required.
- These models are inviscid, and therefore, the drag information is required and the vortex/wake decay is either ignored or modeled.
- Since the blade is represented as a lifting line, the surface information is lost, and hence effects due to the blade thickness and vortex-surface interaction cannot be captured.

Compressible Reynolds Averaged Navier–Stokes (RANS) solver can be used to study the performance and flow physics of a coaxial rotor. In this approach, the use of higher level approximation of the fluid flow equations coupled with an accurate representation of the blade geometry can provide further insight into the aerodynamics and performance of the coaxial system. It has to be recognized however, that a different set of challenges are involved in such a simulation. A major difficulty in RANS-based CFD simulations of the coaxial rotor computations is the enormous computational cost required to handle the counter-rotating system. Additionally, in order to capture the blade-vortex and vortex-vortex interactions correctly, it is important to accurately represent the formation and evolution of the wake. Hence, accurate numerical schemes and reliable turbulence models need to be used and the resulting methodology needs to be carefully validated with experiments if the CFD results are to be considered reliable.

Recently, Duraisamy & Baeder (Refs. 10, 11) used the high order accurate overset RANS code, OVERTURNS, to simulate the single bladed hovering rotor experiment of Martin et al (Ref. 12). For the first time, detailed validations of the swirl and axial velocities were achieved up to one full revolution of the wake (roughly 60 chords of evolution). In addition, the aerodynamic loading was validated on single rotor systems.

In a previous work (Ref. 13) by the current authors, initial steps were taken to extend the application of this methodology to a coaxial rotor system by simulating a hovering coaxial rotor and validating with the experimental results. In the study, the overall performance was predicted reasonably well. The performance of the top rotor was similar to that of a single rotor, but the bottom rotor showed a degradation of performance due to the influence of the top rotor wake. The computed performance data showed that the flow field of a coaxial rotor is unsteady with a dominant 2N/rev (N = 2) frequency. As a result of the finite thickness of the blade surfaces, the integrated thrust and power showed an impulsive behavior when the blades of the top and bottom rotor were aligned. Additional impulsiveness was generated due to the blade loading. However, as opposed to the experiment, the computed solutions were not fully trimmed. Moreover, the meshes used were relatively coarse and probably were not sufficient to accurately represent the unsteady interactions in the wake.

The goal of the present work is to improve the results of the previous work and provide a better understanding of the flow physics of a hovering coaxial rotor. The present work seeks to improve upon the previous calculations in the following manner :

- All computations will be performed on a finer mesh, which should help in capturing the wake more accurately. Additional benefits will be gained by using a smaller time step size.
- Higher order sliding mesh boundary interpolation will be used. Previously, a first order (linear) interpolation was used. For the present work, third order slope limited M3-quartic interpolation of Huynh (Ref. 14) is implemented. This should again aid in better wake capturing.
- A trim procedure will be implemented to balance the torque and to trim the thrust to a particular value. The experimental results are torque-trimmed and therefore, it is appropriate to trim the CFD solution for the purpose of comparison.

## Methodology

The computations are performed using the compressible RANS solver OVERTURNS (Ref. 10). To allow for adequate mesh resolution and ease of grid generation, structured overset meshes are used. Time integration is performed using the second order implicit Backwards Difference method scheme with Lower-Upper Symmetric Gauss-Siedel (LUSGS) method (Ref. 15) for inversion. In hovering single rotor calculations, it is typical to solve the Navier-Stokes equations in the rotating reference frame (Ref. 16) such that a steady solution is sought. However, the inherently unsteady nature of the flow field in the current work requires the use of time-accurate calculations. Therefore, in this paper, all the computations (including the single rotor calculations) are performed in a time-accurate manner in the inertial frame of reference.

The LUSGS inversion is used along with 6 Newton subiterations (Ref. 17) to remove factorization errors and to recover time accuracy. The chosen time-steps corresponds to 0.125° of azimuth. The inviscid spatial terms are computed using a third order MUSCL scheme with Roe's flux difference splitting and the viscous terms are computed using second order central differencing. The Spalart-Allmaras (Ref. 18) turbulence model is employed for the RANS closure. This one-equation model has the advantages of ease of implementation, computational efficiency and numerical stability. The production term in this eddy-viscosity model is modified (Ref. 10) to account for the reduction of turbulence in the vortex core due to flow rotation effects. The downwash velocity in the bottom plane of the rotor can be significant. In order to account for this and to properly represent the inflow at the other far-field boundaries, the point-sink boundary condition approach of Srinivasan et al. (Ref. 16) is used for both single and coaxial rotor systems.

# Single Rotor Validation

This section describes the computations performed on various two-bladed experimental setups. The measurements of McAlister et al. (Ref. 19) and Harrington (Ref. 20) were chosen to demonstrate the capability of OVERTURNS to predict the overall performance and the setup of Caradonna and Tung (Ref. 21) is used to to validate surface pressure distributions. A two mesh overset system with a body-conforming blade mesh and a cylindrical background mesh are used for all the cases. The periodicity of the flow-field is utilized and hence, only half the computational domain is simulated.

## Caradonna rotor [Surface pressure prediction]

The experimental setup consists of a two-bladed rigid rotor in a hover chamber. The blades have a rectangular planform and are untwisted with a radius of 1.143m. The aspect ratio of the blade is 6. The blades use a NACA0012 airfoil section along the entire span. A precone angle of 0.5° was set for the blades. Validations were done for the case with blade collective of 8°. The tip Reynolds number is $1.96 \times 10^6$ and the tip Mach number is 0.439. The blade mesh has $267 \times 155 \times 111$ points in the streamwise, spanwise and normal directions, respectively and the background cylindrical mesh has $127 \times 186 \times 198$ points in the azimuthal, radial and vertical directions, respectively.

Figure 1 shows the blade pressures at various spanwise locations. It is seen that the computations agree well with the measured distributions.

## McAlister rotor [Thrust/Power prediction]

The experimental setup consists of a two-bladed rigid rotor with an aspect ratio of 6. The profile of the blade is a NACA0020 airfoil at 0.2R that linearly tapers to a NACA0012 at 0.5R. The profile remains a NACA0012 from 0.5R to 1.0R. The blade is set at a collective of 8°. Validation is done for the case with Reynolds number of $1.6 \times 10^6$ and the tip Mach number of 0.387. The blade mesh has $267 \times 155 \times 111$ points in the streamwise, spanwise and normal directions, respectively and the background cylindrical mesh has $127 \times 186 \times 198$ points in the azimuthal, radial and vertical directions, respectively (see Fig. 2). The experimental value of $C_T$ and $C_Q$ are reported as 0.00500 and 0.000500, respectively. The predicted values of $C_T$ and $C_Q$ are 0.00480 and 0.000512, respectively. The comparison shows that OVERTURNS gives a reasonable performance prediction for a single two-bladed rigid rotor configuration.

## Harrington rotor [Performance prediction]

Harrington conducted experiments on two different rotors in both single and coaxial rotor configurations. The experimental data (referred to as Rotor-2) is used to validate both single and coaxial rotor systems. The experimental setup consists of a two-bladed rigid rotor with an aspect ratio of 8.33. The blade uses a NACA airfoil with a linearly varying thickness of 27.5% at $0.2R$ to 15% at $R$. The tip Reynolds number is $3.5 \times 10^6$ and the tip Mach number is 0.352. Different collective pitch settings from 4° to 12° were used to obtain the variation of thrust with power. The blade mesh has $267 \times 78 \times 56$ points in the streamwise, spanwise and normal directions, respectively and the background cylindrical mesh has $97 \times 135 \times 118$ points in the azimuthal, radial and vertical directions, respectively. Performance quantities were found to be insensitive to further mesh refinement for the isolated rotor.

Figure 3(a) shows the computed performance along with the experimental results. The results are reasonably good with a slight over-prediction of power at lower collective pitch settings and minor under-prediction of power at higher collectives for a given thrust. The induced power and the profile power can be isolated to first order by calculating the power due to the pressure forces and the viscous forces separately. Figure 3(b) shows the variation of the computed induced and profile power coefficient with the thrust coefficient. As expected, the profile power remains constant, while the induced power increases with the thrust. Plotted along with the experimental data and the CFD results is the curve fit using momentum theory ($C_Q = \frac{kC_T^{3/2}}{\sqrt{2}} + \frac{\sigma cd_0}{8}$). The value of $k = 1.25$ and $cd_0 = 0.013$ is used for the fit.

## Coaxial Rotor Validation

Hovering coaxial rotor simulations can be simplified if cylindrical background meshes are used. The periodicity of the flow-field can be utilized by incorporating the sliding mesh interface condition between the two rotor systems, allowing for a complete simulation using just one blade mesh in each rotor system. Figure 4 shows a schematic of the blade surfaces and the blade and background mesh boundaries. The solid lines show the meshes for the simulated blade and the dotted lines depict periodicity. The sliding boundary condition for the simulated background mesh of any of the two rotors is implemented by exchanging information with either the simulated background mesh or the periodic mesh of the other rotor. This type of interface condition, though novel in helicopter calculations, is routinely used in simulations of gas turbine rotor-stator flow-fields.

As mentioned earlier, the coaxial experimental setup of Harrington Rotor-2 (Ref. 20) is used to validate the computational predictions. It consists of two 2-bladed rotors arranged to form a coaxial system. The rotors are similar to the one used in single rotor setup. The solidity of each of the rotors is 0.076 with rotor spacing, H/D = 0.08 (1.33 chords).

A four mesh system consisting of two blade meshes and two cylindrical background meshes was used. The blade mesh and the background mesh of each rotor form an overset system. The background meshes communicate with each other by means of a sliding mesh interface as explained earlier. The solution is transferred from one mesh to the other by using a third order slope limited M3-quartic interpolation of Huynh (Ref. 14). This is an improvement from the previous work (Ref. 13), where only a first order (linear) interpolation was used. Apart from providing a better representation of the wake, the improved interpolation significantly reduces the oscillations in the forces of the bottom rotor arising due to the interpolation error, see Fig. 5, which shows a plot of $C_T$ and $C_Q$ versus azimuth for the bottom rotor for case 7 (see Table 1). It should be mentioned here that, spectral scheme was investigated to provide higher order interpolation. However, the results were unsatisfactory due to the presence of numerous spurious oscillations and therefore, in order to minimize these oscillations, a monotonic M3-quartic interpolation was chosen. The extra cost for the higher-order interpolation is minimal since the interpolation is only one-dimensional between the sliding mesh boundaries.

With the exception of the 0° collective setting case, all the computations are performed on top and bottom rotor blade meshes having $267 \times 155 \times 111$ points in the streamwise, spanwise and normal directions, respectively, top rotor background mesh having $97 \times 270 \times 61$ points and bottom rotor background mesh having $97 \times 270 \times 180$ in the azimuthal, radial and vertical directions, respectively. Total number of mesh points used is 15.7 million. For the 0° collective setting case, where there is no significant wake to be captured, the computations are performed on a coarser mesh system obtained by leaving out every other point in the spanwise and normal directions. Recall the earlier mention that in the previous work by the present authors (Ref. 13), reasonable performance results were obtained for all collective settings using the coarse mesh.

Figure 6 shows the blade and cylindrical meshes. The blade mesh of the top rotor is sufficiently fine in the tip region to resolve the tip vortex formation. For the bottom rotor, the grid is redistributed such that the inboard region is highly refined in order to resolve the wake interaction. In the most refined regions, the background mesh has a grid spacing of 0.02 chords and 0.033 chords, respectively in the radial and the vertical directions. Along the azimuthal direction, a grid plane is spaced every 2°. The outer boundary of the background mesh extends to 1.5R above the top rotor, 3R below the bottom rotor and 1.5R from the tip of the blade.

## Trimming Procedure

In the experimental test, the top and bottom rotors were torque balanced by selecting the appropriate collective pitch. In order to obtain a reasonable validation, the CFD results need to be yaw-trimmed. This is achieved by using a trimming procedure, by which the thrust is trimmed to a specific value in addition to balancing the torque. The CFD calculations are started using initial collective settings obtained from the vortex filament method for various target values of thrust. These settings were provided by Ananthan (Ref. 2). The results obtained using these settings are presented in the previous work (Ref. 13) of the current authors. The difference in the rotor powers was seen to be around $10\% - 12\%$ of the total power. The reason for this is the inconsistency between the CFD and vortex filament methods. Using these initial results, the collective settings are changed in a manner described below (Ref. 22).

The rotor control input vector and the response vector are respectively given by

$$\begin{aligned} \mathbf{x} &= \{\theta_{0_1}, \theta_{0_2}\}^T \\ \mathbf{y} &= \{\Sigma C_T, \Sigma C_Q\}^T \end{aligned}$$

where, $\theta_{0_1}$ and $\theta_{0_2}$ are respectively the collective setting of the top and bottom rotor. Note that the sign of $C_Q$ of the bottom rotor is taken negative.

The change in the response vector for a perturbation in the input vector $\mathbf{x}$ can be written as a Taylor series expansion given by

$$\mathbf{y}(\mathbf{x}+\Delta\mathbf{x}) = \mathbf{y} + \frac{\partial \mathbf{y}}{\partial \mathbf{x}}\Delta\mathbf{x} + \ldots$$

The Jacobian matrix, $[J]$ of the dependent quantities with respect to the independent quantities can be written as

$$[J] = \frac{\partial \mathbf{y}}{\partial \mathbf{x}} = \begin{bmatrix} \frac{\partial \Sigma C_T}{\partial \theta_{0_1}} & \frac{\partial \Sigma C_T}{\partial \theta_{0_2}} \\ \frac{\partial \Sigma C_Q}{\partial \theta_{0_1}} & \frac{\partial \Sigma C_Q}{\partial \theta_{0_2}} \end{bmatrix}$$

Neglecting the higher order terms, the expression for the perturbation in the control input vector $\mathbf{x}$ can be written as

$$\Delta\mathbf{x} = [J]^{-1}(\mathbf{y}(\mathbf{x}+\Delta\mathbf{x}) - \mathbf{y}) = [J]^{-1}\left\{ \begin{array}{c} \Sigma C_T - C_{T_{req}} \\ \Sigma C_Q \end{array} \right\}$$

The Jacobian matrix obtained from the vortex filament code is used to determine the change in collective settings. The solution for the new collective settings are calculated using the previous solution as the initial condition. As a result, the convergence time reduces significantly, thereby making the trimming procedure feasible. The above step is repeated until the values are trimmed to within 1% of the target. For all cases the trim criteria was met in 3 to 4 iterations.

Table 1 shows the trim collective settings obtained for various target thrust values. These settings are not too different from that obtained using vortex filament code. Also, notice that the collective setting of the top and bottom rotor are not significantly different.

## Performance Comparison

### Mean Performance

Tables 2 and 3 respectively summarize the mean values of thrust ($C_T$) and power ($C_Q$) coefficients obtained from CFD for individual rotors as well as for the entire system. It can be seen that all the cases are trimmed to within the specified criteria of 1% error. Looking at the thrust values, we can observe a general trend that as the total thrust increases, the difference between the top and bottom rotor thrust also increases. Table 2 also shows the ratio of the top rotor thrust to the total thrust. At lower thrust levels, the top rotor shares higher percentage of the total thrust. As the thrust increases, the thrust share becomes more balanced, with the top rotor contributing to about 55% of the total value.

Figure 7(a) compares the computed variation of mean total thrust coefficient with mean total power coefficient with the measured values. The total performance is well predicted. At lower collectives, the power is slightly over-predicted for a given thrust, whereas at higher collectives, the power is marginally under-predicted for a given thrust level. This is similar to that presented earlier for the isolated rotor. Plotted along with the experimental data and the CFD results is the curve fit using momentum theory for coaxial rotor (Ref. 3) ($C_Q = \frac{k\ k_{int} C_T^{3/2}}{2} + \frac{2\sigma c d_0}{8}$), where $k_{int}$ is the interference factor, $\sigma$ is the solidity of single blade. The value of $k = 1.25$ and $cd_0 = 0.0013$, which is obtained from the single rotor results, is used. The value of $k_{int} = 1.35$ is used for the fit. Leishman (Ref. 3) has shown that for ideal case, when the bottom rotor operates in the vena-contracta of the top rotor, the value of $k_{int}$ is 1.281. The slightly higher value of $k_{int}$ accounts for the non-ideal contraction of the top rotor wake.

The induced and the profile component of the power can be isolated to first order by calculating the power due to the pressure and viscous forces separately. Both these components of power are plotted in Fig. 7(b), along with the curve fit using momentum theory. As expected the profile power coefficient remains constant, equal to $\frac{2\sigma c d_0}{8}$, as the thrust increases. The induced power coefficient increases with thrust.

Figure of merit (FM) is defined as the ratio of the ideal power to the actual power (Ref. 3).

$$FM = \frac{C_{Q_{ideal}}}{C_{Q_{actual}}} = \frac{\frac{k_{int} C_T^{3/2}}{2}}{C_{Q_{actual}}}$$

where $k_{int}$ is the ideal interference factor, equal to 1.281. Figure 7(c) shows the plot of figure of merit versus mean thrust coefficient. As the thrust increases, the FM increases, reaching a value of above 0.55 for case 9.

Figure 7(d) shows the mean performances of individual rotors (zero collective case is excluded). It is interesting to note that the performance of the top rotor is very similar to that of a single rotor. However, for the bottom rotor, the performance degrades because of the influence of the wake from the top rotor.

### Unsteady Performance

A measure of the unsteadiness in thrust and power is the root mean square value of the temporal variations and this is summarized in Tables 4 and 5. As a general trend, the absolute value of the fluctuation increases with increasing collective pitch settings, however, the relative fluctuation with respect to the mean value is seen to decrease for all quantities except the top rotor power. For the top rotor power, relative fluctuation is seen to remain constant over a large range of $C_T$. Additionally, when the fluctuations of the whole system is compared to that of the individual rotors, it is seen that though the absolute value is higher, the relative fluctuation is smaller. Further details of the temporal variation will be presented later in this section.

Figure 8 shows the temporal variation of $C_T$ and $C_Q$ over one revolution for case 7. Note that, when viewed from above, the top rotor rotates in an anti-clockwise fashion and the bottom rotor rotates clockwise. Therefore, the azimuthal locations of the top and bottom rotors are measured in their respective directions of rotation. From the figure, the unsteadiness is clearly seen with a dominant 4/rev frequency (number of times a blade of one rotor encounters a blade of the other rotor in one revolution). A higher frequency variation can be seen in the form of spikes when the blades are very close to each other. Such a variation can be attributed to the venturi effect caused by the thickness of the blades, which leads to a reduction in pressure between the rotors. As a result, the thrust of the top rotor spikes down whereas the thrust of the bottom rotor spikes up. Apart from the venturi effect, there is also an upwash-downwash effect created by the bound circulation of the blades. These effects are schematized in Fig. 9. As the blades of the top and bottom rotors approach each other, each of the blades induce an upwash on the other blade. The upwash increases as the blades approach each other, but after a certain point it starts decreasing, changes sign and acts as a downwash. The strength of the downwash is seen to initially increase and then starts decreasing as the blades move away from each other. Correspondingly, the forces on both the top and the bottom rotor increase as the blades approach, then decrease and then increase again as they move away. Furthermore, while the thrust and the power of the top rotor show an impulsive but phased behavior, for the bottom rotor which lies in the wake of the top rotor, the features are more spread out and distinct. Figure 8(c) shows the temporal variation of the induced and the profile component of $C_Q$ for both the rotors. The profile component of the power coefficient is almost constant with time and is equal for both the rotors. Figure 8(d) shows the temporal variation of the fraction of the total thrust shared by the top rotor. For most of the time, the fraction is close to the average value of $0.57$. When the blades pass each other, the ratio briefly peaks to a value more than $0.6$ and then impulsively dips to a value less than $0.5$.

Compared to the previous work (Ref. 13), the present calculations show larger unsteadiness for the bottom rotor. Additional higher frequencies are observed and the root mean square values of the temporal variation of the integrated quantities are higher. There exists a secondary hump in the temporal variation of $C_T$ and $C_Q$ of the bottom rotor. These features are captured mainly as a result of using finer mesh, because of which the wake of the top rotor is better preserved. Additionally, the implementation of higher order sliding mesh interpolation and also the use of smaller time step size contribute in capturing the wake more accurately.

The unsteadiness in the flow can be better quantified by investigating the frequency content in the integrated quantities. In Fig. 10, the amplitude of the discrete frequency components of $C_T$ and $C_Q$ of the top and bottom rotor, normalized by the amplitude of the 4/rev frequency component of the respective quantity of the top rotor, is plotted. It is seen that in all the cases (except the top rotor power), 4/rev is the dominant frequency. For the top rotor power, the dominant frequency is 12/rev. The presence of these higher frequencies is due to the sharper nature of the impulses. Comparing the frequency components of the top and bottom rotor quantities, we observe that as a result of the greater unsteadiness in the flow field of the bottom rotor, the 4/rev components of the bottom rotor are much larger. However, the integrated quantities are more impulsive for the top rotor compared to that of the bottom rotor and therefore the bottom rotor has relatively smaller higher frequency contents.

Figure 11 shows the temporal variation of thrust and power for the zero collective case. From the figure, it can be seen that, at all times, the top and bottom rotors produce almost equal and opposite thrust resulting in a net zero thrust, while the power of both rotors are almost identical. This behavior is expected, because for this zero collective case, the loading and wake effects are negligible and only the venturi effect is prominent. Therefore, for both top and bottom rotors, the forces remain constant for most of the time, being impulsive only when the blades pass each other.

Figure 12 shows the temporal variation of $C_T$ and $C_Q$ over one revolution for cases 2-9. As the collective pitch is decreased, the peak of the bottom rotor forces, which is expected to occur when the tip vortex from the top rotor interacts with the bottom rotor, moves to a later azimuth. This is a result of the decreased inflow leading to a slower vertical convection of the tip vortex.

Figure 13 shows the spanwise lift distribution for both the top and the bottom rotors at different azimuthal locations for case 7. For the top rotor, the lift distribution is similar at all azimuth locations except $0^\circ$. At $0^\circ$ azimuth, due to the venturi effect discussed earlier, the lift is lower. For the bottom rotor, the lift varies significantly with azimuth. A dip is noticeable in the lift distribution of the bottom rotor at various azimuth locations. This is due to the interaction of the tip vortex from the top rotor with the bottom rotor (as will be evident from the flow visualization results). The relative location of the dip suggests that that the wake of the top rotor has contracted to $0.8R$.

An azimuthal contour of the sectional lift ($c_l M^2$) and its fluctuation from the mean value are respectively plotted in Figs. 14 and 15, for both the top and bottom rotors. The figures clearly show the large fluctuations in the outer portions of the rotors as they pass by each other, as well as the additional unsteadiness on the bottom rotor as the wake from the top rotor encounters the plane of the bottom rotor.

### Wake Trajectory

Figure 16 shows the wake trajectory for case 7 when the top and bottom rotor blades are aligned with each other. The radial contraction of the wakes with the azimuth is plotted in Fig. 16(a). It can be seen that the wake of the top rotor contracts at a much faster rate compared to that of the bottom rotor. This is a result of the interaction between the two wakes, which forces the top rotor wake inward, while pushing the bottom rotor wake outward. Figure 16(b) shows the vertical convection of the wakes with the azimuth. Clearly, the wake of the top rotor convects at a faster rate due to the presence of increased inflow. Both the wakes show increased vertical convection rate after the first blade passage at 180° azimuth. Figure 16(c) shows the spatial location of both the wakes. It can be seen that the wake of the top rotor contracts to about $0.8R$ by the time it reaches the bottom rotor.

### Flow-field Visualization

Figure 17 shows the vorticity magnitude contours for case 7 in a fixed plane in space at various instances in time. At the first instance both the top and bottom rotor blade are aligned at the plane. As the time increases, the wake age of both the top and bottom rotor tip vortices at this plane increases. At the early wake ages, the top and bottom rotor tip vortices can be clearly distinguished. As the wake age increases, the vortices interact with each other and also with the inboard sheet, resulting in a very complicated flow-field.

Figure 18 shows the vorticity magnitude contours for case 7 in a plane that is at 30° azimuth with respect to the top rotor blade, at different instances in time. At this plane, wake age of the tip vortices trailed from the top rotor remains constant, while the wake age of those trailed from the bottom rotor increases. At the first instance, the top and the bottom rotor blades are aligned. At a later time, the bottom rotor blade can be seen to intersect the plane of interest. From these plots we can observe that, even though the vortices trailing from the top rotor vortices are at constant wake age, they are not at a fixed position. Due to the various vortex-vortex and blade-vortex interactions, the tip vortices trailing from the top rotor (especially the ones after the first blade passage) shows significant wandering. Figure 19 shows the vorticity magnitude contour for case 7, but in a plane that is at 30° azimuth with respect to the bottom rotor blade. At this plane, the wake age of the bottom rotor vortices are fixed and the wake age of the top rotor vortices increases. Again, significant wandering of the bottom rotor tip vortices can be seen.

In order to extract only the rotational flow regions and not the highly strained regions, the so-called q-criterion (Ref. 23) is shown in Fig. 20(a). The tip vortices are resolved for two blade passages. Beyond this wake-age, the background mesh becomes too coarse to accurately represent the details of the tip vortex. After passing the bottom rotor, there is a significant interaction between the tip vortices. Figure 20(b) shows the tip vortex from the top rotor passing close to the bottom rotor. It is clearly seen that even after the interaction, the tip vortex from the top rotor remains coherent. There is also some evidence of straining in the tip vortex from the preceding bottom rotor blade as it passes slightly under the subsequent bottom rotor blade.

## Conclusions

A compressible Reynolds Averaged Navier Stokes (RANS) solver was applied to simulate the aerodynamics of single and coaxial rotor configurations in hover. The computations were performed on structured body-conforming blade meshes, overset in a cylindrical background mesh. The computations were validated with experimentally measured mean thrust and power and the sources of unsteadiness were examined. The following are specific conclusions that can be drawn from the present work :

- The validation studies for a single rotor system show good agreement with the experimental performance and pressure distribution data.

- A trim procedure was implemented to trim the coaxial system to a particular thrust value and to balance the torque. Trimming was achieved to less than 1% error.

- A higher order one-dimensional sliding mesh interpolation scheme was implemented, which aided in the reduction of spurious oscillations generated in the integrated quantities of the bottom rotor due to interpolation errors.

- The overall performance is predicted reasonably well for the coaxial system. The performance of the top rotor was similar to that of a single rotor, but the bottom rotor showed a degradation of performance due to the influence of the top rotor wake.

- The top rotor shares significantly large fraction of the total thrust at lower thrust levels. At higher thrust values, the sharing becomes more balanced and the fraction reduces to about 55% of the total thrust.

- The computed performance data showed that the flow-field of a coaxial rotor is unsteady with a dominant 4/rev frequency. As a result of the finite thickness of the blade surfaces, the integrated thrust and power showed an impulsive behavior when the blades of the top and bottom rotor were aligned. Additional impulsiveness is generated due to the blade loading. For the bottom rotor, the added influence of the top rotor wake makes the features more spread out and distinct.

- The profile component of the power remains constant for various thrust levels and also with time for a particular thrust level for both top and bottom rotor. The value of the total profile power coefficient of the coaxial system is close to $\frac{2\sigma cd_0}{8}$, where the value of $cd_0$ is same as that obtained for single rotor.

- The induced component of the total power can be fit using momentum theory by accounting for the interference between two rotors. The interference factor $k_{int}$ was obtained as 1.35, which is higher than the ideal value of 1.281. The higher value accounts for the non-ideal wake contraction of the top rotor.

- The wake of the top rotor contracts at a faster rate compared to that of the bottom rotor because of the vortex-vortex interaction. The top rotor wake contracts to about $0.8R$ by the time it reaches the bottom rotor. Additionally, the top rotor wake convects vertically down at a faster rate due to increased inflow.

- The tip vortices from both the top and bottom rotor blades were preserved until two blade passages. It was observed that the tip vortex from the top rotor passes very close to the bottom rotor blade. This interaction, along with that between tip vortices from the top and bottom rotors, produce a highly complicated flow field.

# Future Work

The primary focus of the present work was on the prediction of hover performance and to do an in-depth study of the flow physics of a coaxial system using CFD. As a continuing work, the effects of the fuselage or a ground plane can be included. Once the hovering condition is fully studied, CFD computations can be performed in forward flight.

# Acknowledgments

This work was funded by the National Rotorcraft Technology Program under the "Detailed CFD Simulations of Hovering Multi-Rotor Systems" project (2007-B-11-01.2-A9). The authors are also greatly appreciative of Dr. Shreyas Ananthan (Ref. 2) for providing the initial collective settings of the Harrington coaxial rotor-2 setup and for helping with the vortex filament method code.

# References

[1] Coleman, C. P., “A Survey of Theoretical and Experimental Coaxial Rotor Aerodynamic Research,” Proceedings of the 19th European Rotorcraft Forum, Como, Italy, September 14–16, 1993.

[2] Leishman, J. G., and Ananthan, S., “Aerodynamic Optimization of a Coaxial Proprotor,” *62nd Annual Forum of the American Helicopter Society,* 2006.

[3] Leishman, J. G., “Principles of Helicopter Aerodynamics,” Cambridge University Press, 2002.

[4] Leishman, J. G., Bhagwat, M. J., and Bagai, A., ”Free- Vortex Filament Methods for the Analysis of Helicopter Rotor Wakes,” *Journal of Aircraft,* Vol. 39, (5), September-October, 2002, pp. 759-775.

[5] Andrew, M. J., “Coaxial Rotor Aerodynamics,” Ph.D. Thesis, Southampton University, England. c. 1981.

[6] Bagai, A. and Leishman, J. G., “Free-Wake Analysis of Tandem, Tilt-Rotor and Coaxial Rotor Configurations,” *Proceedings of the 51st Annual Forum of the American Helicopter Society,* 1995.

[7] Griffiths, D. A., Leishman, J. G., “A Study of Dual-Rotor Interference and Ground Effect Using a Free-Vortex Wake Model,” *Proceedings of the 58th Annual Forum and Technology Display of the American Helicopter Society International,* 2002.

[8] Nagashima, T. and Nakanishi, K., “Optimum Performance and Wake Geometry of a Coaxial Rotor in Hover,” *Vertica,* vol. 7, pp. 225-239, 1983.

[9] Kim, H. W., and Brown, R. E., “Coaxial Rotor Performance and Wake Dynamics in Steady and Manoeuvring flight,” *Proceedings of the 62nd Annual Forum and Technology Display of the American Helicopter Society International,* 2006.

[10] Duraisamy, K., “Studies in Tip Vortex Formation, Evolution and Control,” Ph.D Thesis, Department of Aerospace Engineering, University of Maryland at College Park, 2005.

[11] Duraisamy, K., Sitaraman, J. and Baeder, J., "High Resolution Wake Capturing Methodology for Accurate Simulation of Rotor Aerodynamics," *61st Annual Forum of the American Helicopter Society,* 2005.

[12] Martin, P. B., Pugliese, G. J., and Leishman, J. G., "High Resolution Vortex Measurements in the Wake of a Hovering Rotor," 57th Annual Forum of the American Helicopter Society Proceedings, Phoenix, AZ, 2001.

[13] Lakshminarayan, V. K., Duraisamy, K. and Baeder, J. D., "Computational Investigation of Coaxial Rotor Aerodynamics in Hover," 63rd Annual Forum of the American Helicopter Society Proceedings, Virginia Beach, VA, 2007.

[14] Huynh, H. T., "Accurate Monotone Cubic Interpolation," *SIAM Journal of Numerical Analysis*, Vol. 30, 1993.

[15] Yoon, S. and Jameson, A., "Lower-Upper Symmetric-Gauss-Seidel Method for the Euler and Navier-stokes Equations," *AIAA Journal,* Vol. 26, 1988.

[16] Srinivasan, G. R., and Baeder, J. D, "TURNS: A Free-wake Euler/ Navier-Stokes Numerical method for Helicopter Rotors," *AIAA Journal,* Vol. 31, No. 5, 1993.

[17] Pulliam, T., "Time Accuracy and the use of Implicit Methods,"*AIAA Paper 1993-3360,* 1993.

[18] Spalart, P. R. and Allmaras, S. R., "A One Equation Turbulence Model for Aerodynamics Flow," *AIAA Paper 92-0439*, 1992, pp. 1–22.

[19] McAlister, K. W., Schuler, C. A., Branum, L. and Wu J. C., "3-D Wake Measurements Near a Hovering Rotor for Determining Profile and Induced Drag." *NASA Technical paper 3577,* 1995.

[20] Harrington, R. D., "Full-Scale Tunnel Investigation of the Static Thrust Performance of a Coaxial Helicopter Rotor," *NACA Technical note 2220,*, 1950.

[21] Caradonna, F. X. and Tung, C., "Experimental and Analytical Studies of a Model Helicopter Rotor in Hover," *NASA TM 81232,* 1981.

[22] Ananthan, S., "Analysis of Rotor Wake Aerodynamics during Maneuvering Flight using a Free-Vortex Wake Methodology," Ph.D Thesis, Department of Aerospace Engineering, University of Maryland at College Park, 2006.

[23] Jeong, J. and Hussain, F., "On the Identification of a Vortex," *J. Fluid. Mech.,* 285, 1995, pp. 69–94.

| Case | $C_T$ (Target) | $\theta_0$ (top rotor) | $\theta_0$ (bottom rotor) |
|---|---|---|---|
| 1 | 0.000 | 0.00° | 0.00° |
| 2 | 0.002 | 4.40° | 4.06° |
| 3 | 0.003 | 5.20° | 5.12° |
| 4 | 0.004 | 6.00° | 6.10° |
| 5 | 0.005 | 6.83° | 6.96° |
| 6 | 0.006 | 7.79° | 7.81° |
| 7 | 0.007 | 8.55° | 8.59° |
| 8 | 0.008 | 9.27° | 9.31° |
| 9 | 0.009 | 10.07° | 10.03° |

Table 1: Trim collective settings for the top and bottom rotors of the coaxial system.

| Case | $C_T$ (top rotor) | $C_T$ (bottom rotor) | $C_T$ (total) | $C_{T_{top}}/C_{T_{total}}$ |
|---|---|---|---|---|
| 1 | $-0.00052$ | 0.00055 | 0.00003 | - |
| 2 | 0.00126 | 0.00072 | 0.00198 | 0.64 |
| 3 | 0.00185 | 0.00116 | 0.00301 | 0.61 |
| 4 | 0.00242 | 0.00161 | 0.00403 | 0.60 |
| 5 | 0.00288 | 0.00210 | 0.00498 | 0.58 |
| 6 | 0.00350 | 0.00252 | 0.00602 | 0.58 |
| 7 | 0.00399 | 0.00305 | 0.00704 | 0.57 |
| 8 | 0.00452 | 0.00350 | 0.00802 | 0.56 |
| 9 | 0.00496 | 0.00400 | 0.00896 | 0.55 |

Table 2: Computed mean $C_T$.

| Case | $C_Q$ (top rotor) | $C_Q$ (bottom rotor) | $C_Q$ (total) | $\lvert C_{Q_{top}} - C_{Q_{bot}} \rvert$ |
|---|---|---|---|---|
| 1 | 0.000121 | 0.000124 | 0.000245 | 0.000003 |
| 2 | 0.000160 | 0.000161 | 0.000321 | 0.000001 |
| 3 | 0.000193 | 0.000193 | 0.000386 | 0.000000 |
| 4 | 0.000225 | 0.000225 | 0.000450 | 0.000000 |
| 5 | 0.000267 | 0.000269 | 0.000536 | 0.000002 |
| 6 | 0.000321 | 0.000319 | 0.000640 | 0.000002 |
| 7 | 0.000370 | 0.000370 | 0.000740 | 0.000000 |
| 8 | 0.000424 | 0.000422 | 0.000846 | 0.000002 |
| 9 | 0.000480 | 0.000482 | 0.000962 | 0.000002 |

Table 3: Computed mean $C_Q$.

| Case | $dC_{T_{rms}}$ (top rotor) | % fluctuation | $dC_{T_{rms}}$ (bottom rotor) | % fluctuation | $dC_{T_{rms}}$ (total) | % fluctuation |
|---|---|---|---|---|---|---|
| 1 | 0.000191 | 36.50% | 0.000194 | 35.40% | 0.000023 | 91.26% |
| 2 | 0.000216 | 17.14% | 0.000160 | 22.22% | 0.000239 | 12.07% |
| 3 | 0.000243 | 13.14% | 0.000190 | 16.38% | 0.000318 | 10.56% |
| 4 | 0.000265 | 10.95% | 0.000198 | 12.30% | 0.000362 | 8.98% |
| 5 | 0.000291 | 10.10% | 0.000242 | 11.52% | 0.000423 | 8.49% |
| 6 | 0.000317 | 9.06% | 0.000299 | 11.87% | 0.000481 | 7.99% |
| 7 | 0.000343 | 8.60% | 0.000336 | 11.02% | 0.000528 | 7.50% |
| 8 | 0.000374 | 8.27% | 0.000356 | 10.17% | 0.000576 | 7.18% |
| 9 | 0.000395 | 7.96% | 0.000394 | 9.85% | 0.000635 | 7.09% |

Table 4: Computed RMS fluctuation of $C_T$.

| Case | $dC_{Q_{rms}}$ (top rotor) | % fluctuation | $dC_{Q_{rms}}$ (bottom rotor) | % fluctuation | $dC_{Q_{rms}}$ (total) | % fluctuation |
|---|---|---|---|---|---|---|
| 1 | 0.0000145 | 11.92% | 0.0000150 | 12.11% | 0.0000295 | 12.01% |
| 2 | 0.0000135 | 8.44% | 0.0000164 | 10.19% | 0.0000267 | 8.32% |
| 3 | 0.0000148 | 7.67% | 0.0000172 | 8.91% | 0.0000270 | 6.99% |
| 4 | 0.0000173 | 7.69% | 0.0000181 | 8.04% | 0.0000295 | 6.55% |
| 5 | 0.0000203 | 7.60% | 0.0000234 | 8.70% | 0.0000355 | 6.62% |
| 6 | 0.0000247 | 7.69% | 0.0000266 | 8.34% | 0.0000402 | 6.28% |
| 7 | 0.0000292 | 7.89% | 0.0000300 | 8.11% | 0.0000441 | 5.96% |
| 8 | 0.0000339 | 7.99% | 0.0000331 | 7.84% | 0.0000479 | 5.66% |
| 9 | 0.0000384 | 8.00% | 0.0000361 | 7.50% | 0.0000533 | 5.54% |

Table 5: Computed RMS fluctuation of $C_Q$.

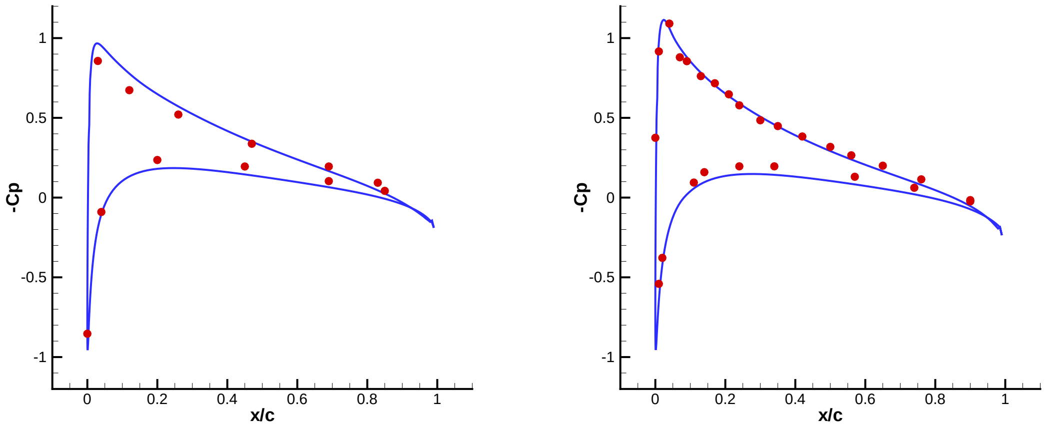

(a) r/R=0.50 (b) r/R=0.80

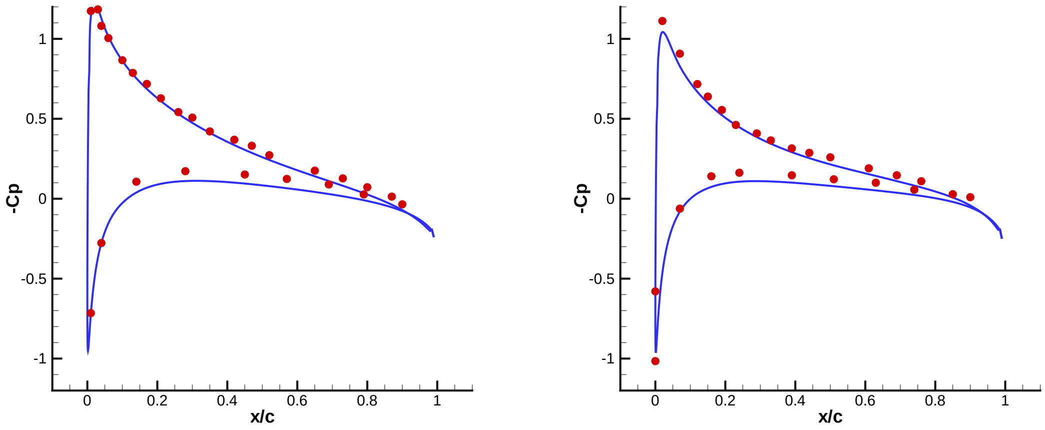

(c) r/R=0.89 (d) r/R=0.96

Figure 1: Comparison of computed blade surface pressure (lines) coefficient with experiment (circles) for Caradonna Rotor.

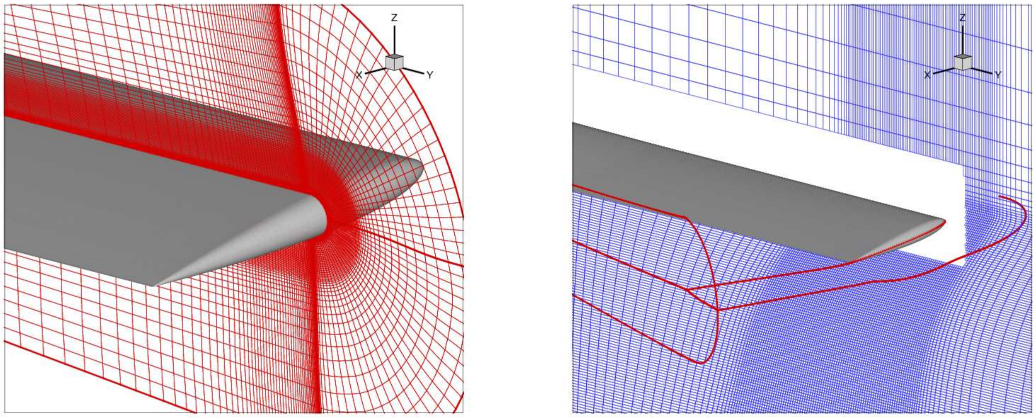

(a) Blade meshes
(b) Cylindrical meshes with blade mesh boundaries

Figure 2: Computational mesh for McAlister rotor.

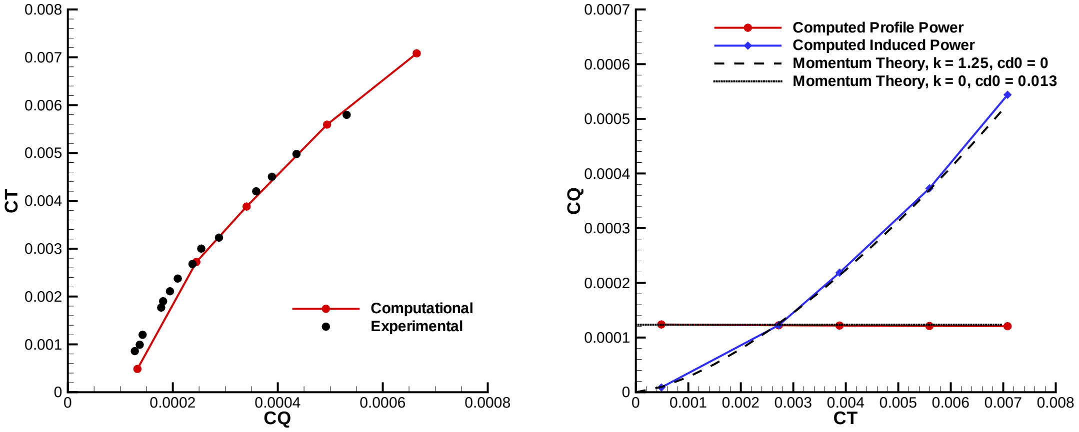

(a)
(b)

Figure 3: Performance comparison for Harrington single rotor.

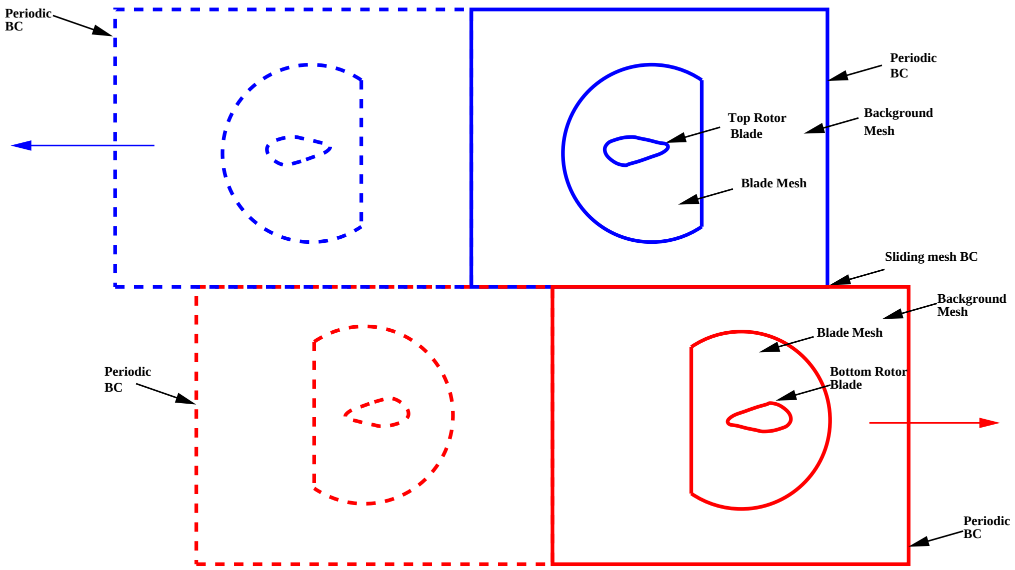

Figure 4: Schematic of the mesh system and the boundary condition for a 2-bladed coaxial rotor.

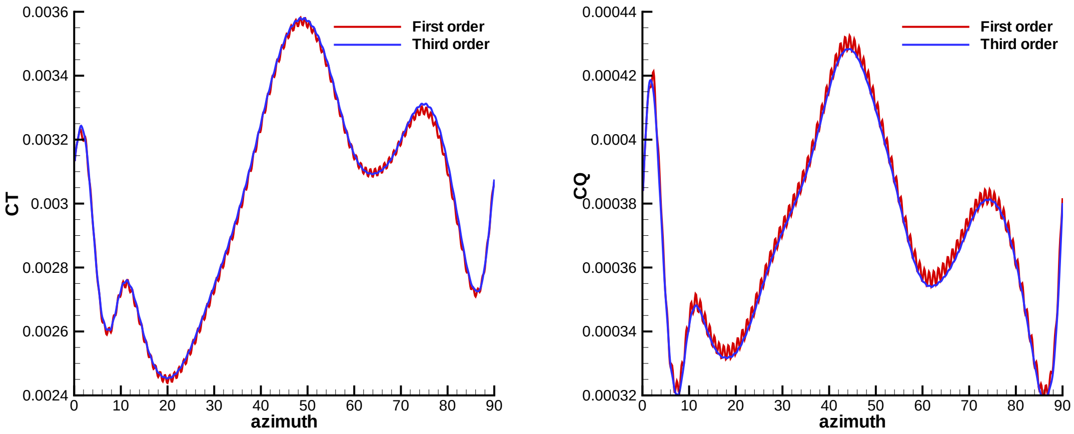

Figure 5: Temporal variation of $C_T$ and $C_Q$ for the bottom rotor of the coaxial system using first and third order sliding mesh interpolation for the coaxial system (case 7).

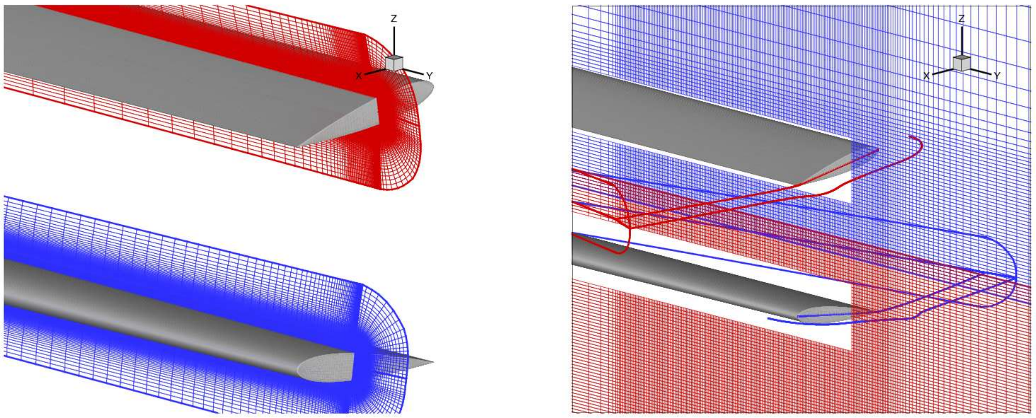

(a) Blade meshes (b) Cylindrical meshes with blade mesh boundaries

Figure 6: Computational mesh for the coaxial rotor system.

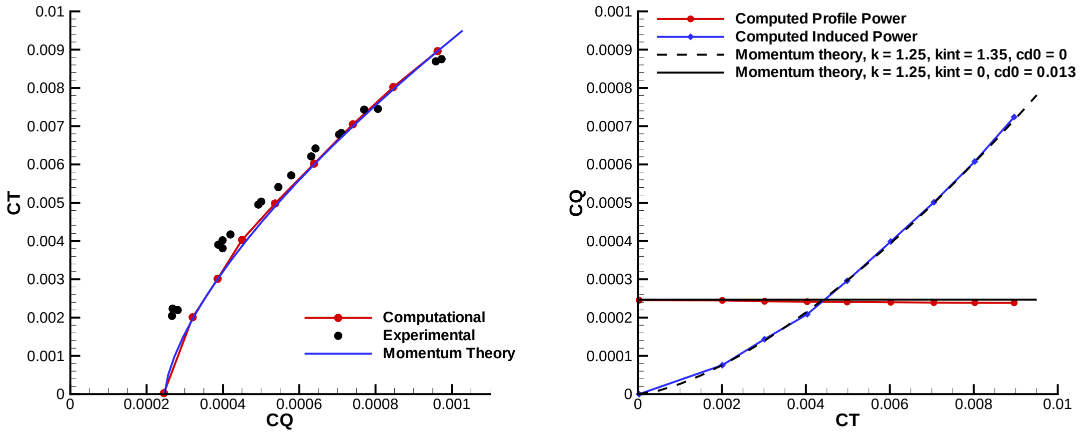

(a) Total $C_T$(mean) versus total $C_Q$(mean) (b) Total induced and profile power (mean) versus total $C_T$(mean)

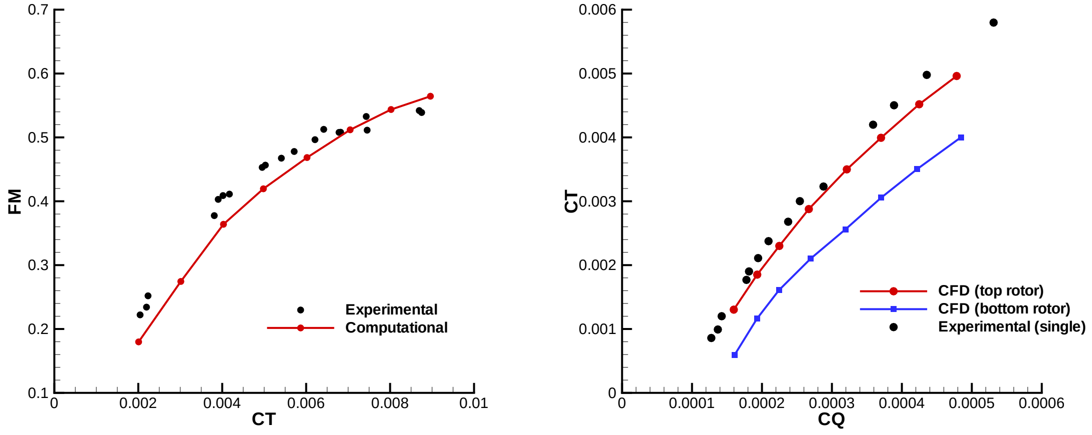

(c) $FM$ versus total $C_T$(mean) (d) $C_T$(mean) versus $C_Q$(mean) for individual rotors.

Figure 7: Comparison of performance for the coaxial rotor.

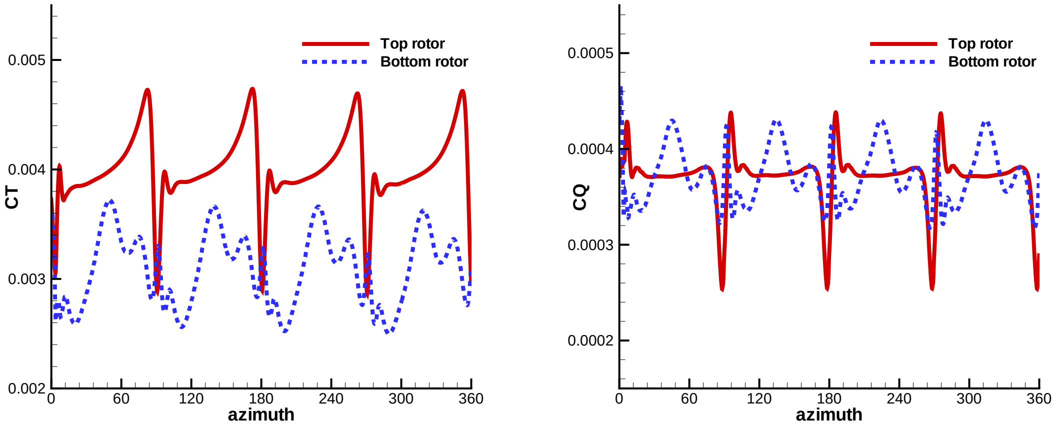

(a) $C_T$ variation

(b) $C_Q$ variation

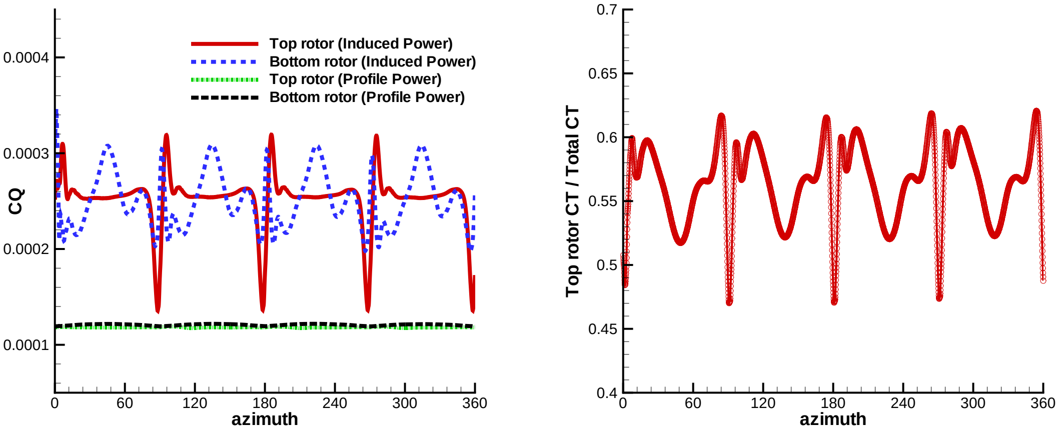

(c) Induced and profile power variation

(d) Ratio of Top Rotor $C_T$ to Total $C_T$

Figure 8: Temporal variation of $C_T$ and $C_Q$ of the top and bottom rotors over one revolution for the coaxial system (case 7).

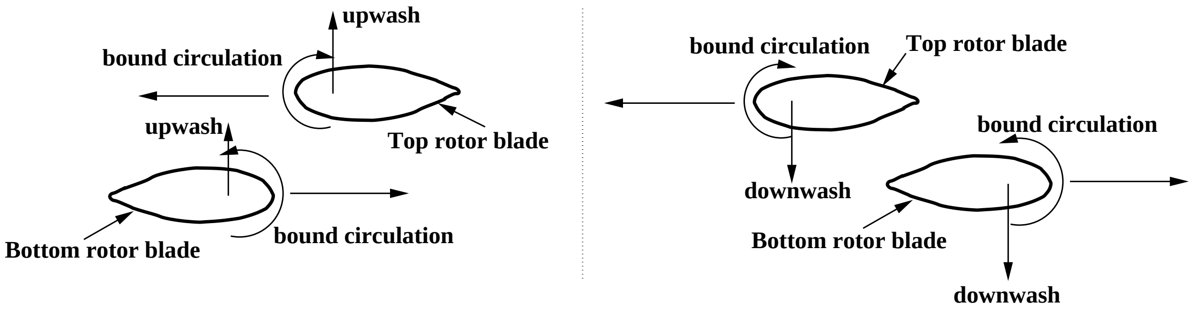

Figure 9: Schematic of the loading (upwash-downwash) effect.

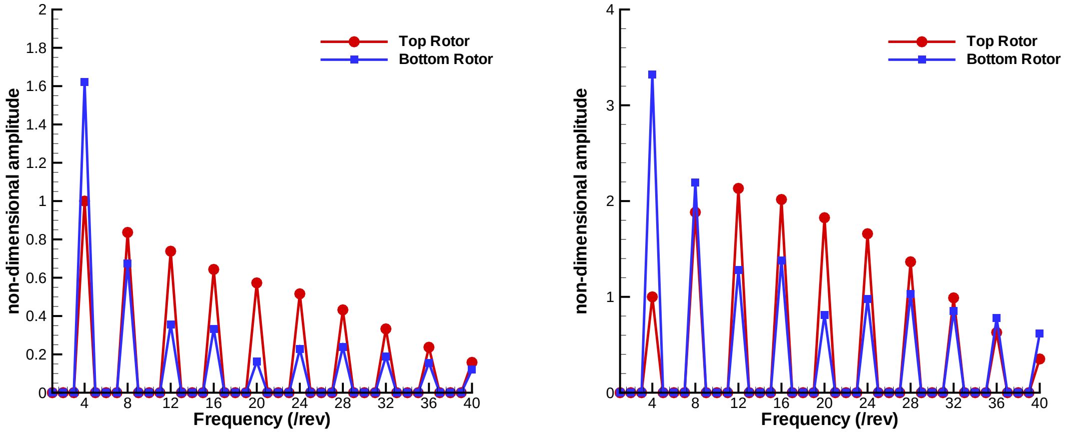

(a) Thrust (b) Power

Figure 10: Frequency distribution, normalized by the amplitude of 4/rev frequency of the top rotor, for the coaxial system (case 7).

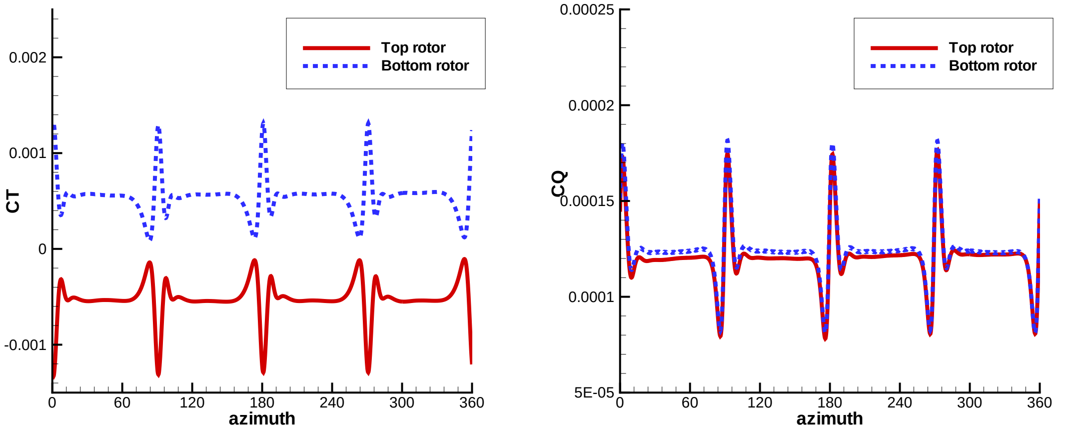

(a) $C_T$ variation (b) $C_Q$ variation

Figure 11: Temporal variation of $C_T$ and $C_Q$ of the top and bottom rotors over one revolution for the coaxial system (case 1).

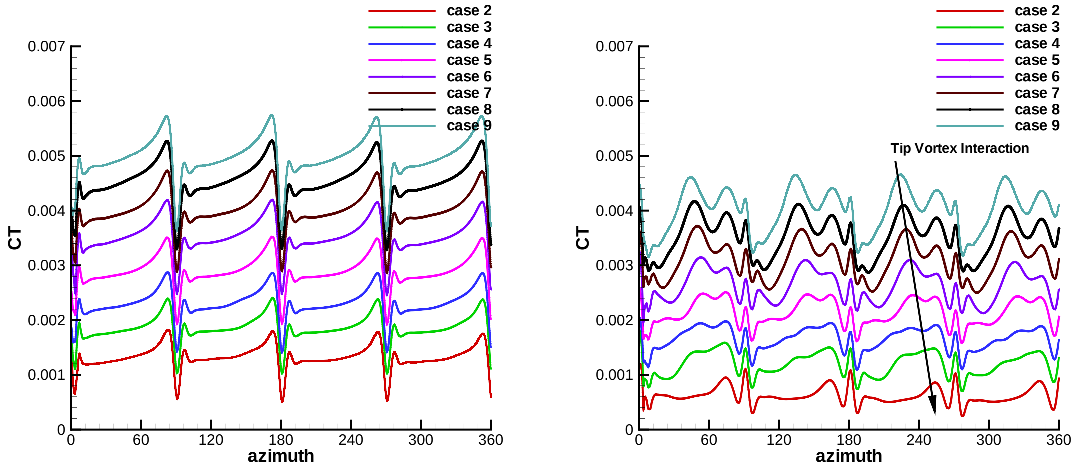

(a) Top rotor $C_T$ variation (b) Bottom rotor $C_T$ variation

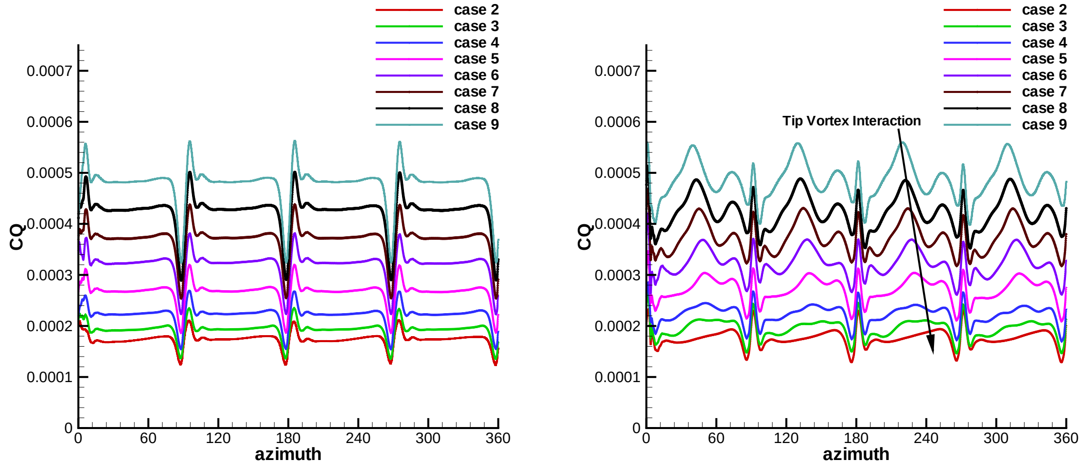

(c) Top rotor $C_Q$ variation (d) Bottom rotor $C_Q$ variation

Figure 12: Temporal variation of $C_T$ and $C_Q$ of the top and bottom rotors over one revolution for all cases for the coaxial system.

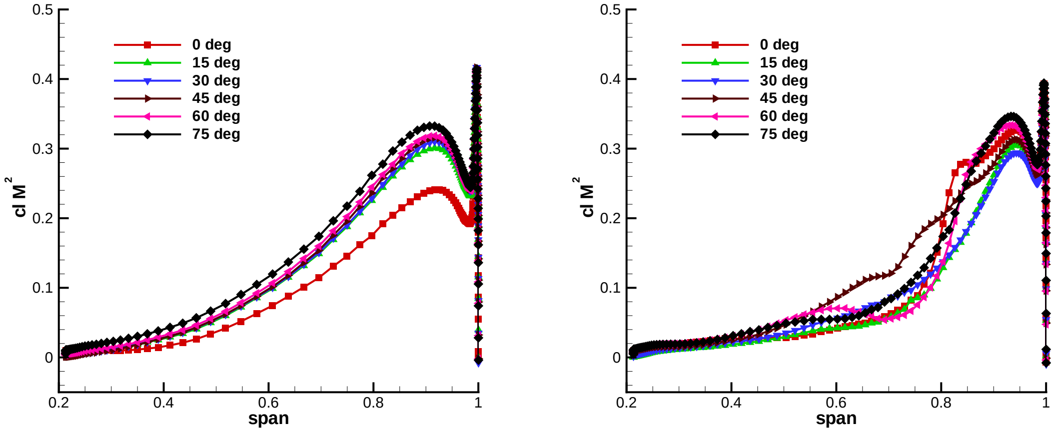

(a) Top Rotor

(b) Bottom Rotor

Figure 13: Spanwise lift distribution at different azimuth locations for the coaxial system (case 7).

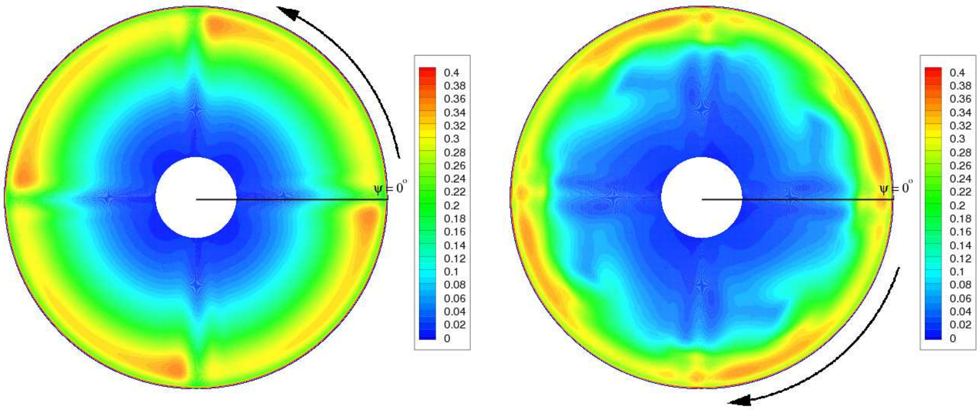

(a) Top rotor

(b) Bottom rotor

Figure 14: Sectional lift ($c_l M^2$) contour for the coaxial system (case 7).

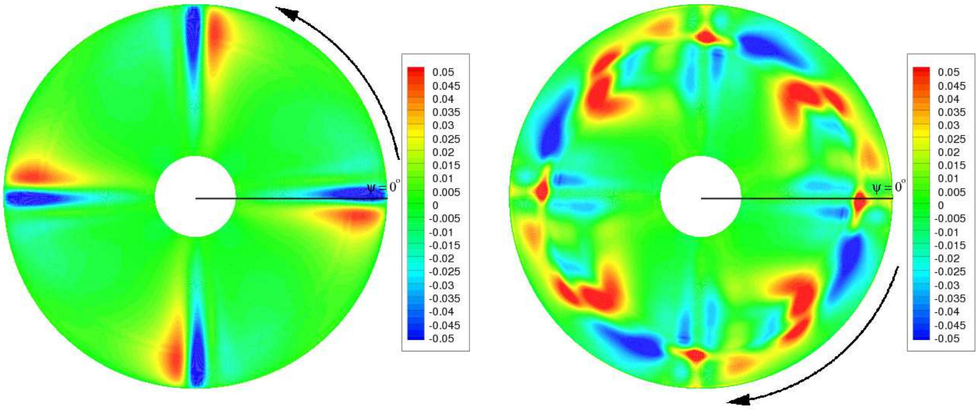

(a) Top rotor

(b) Bottom rotor

Figure 15: Fluctuation in sectional lift ($c_l M^2$) contour for the coaxial system (case 7).

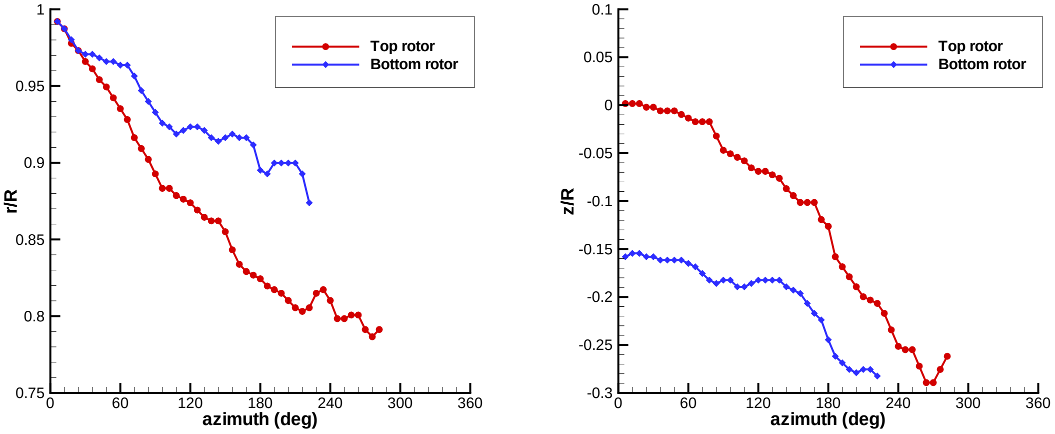

(a) azimuth vs r/R

(b) azimuth vs z/R

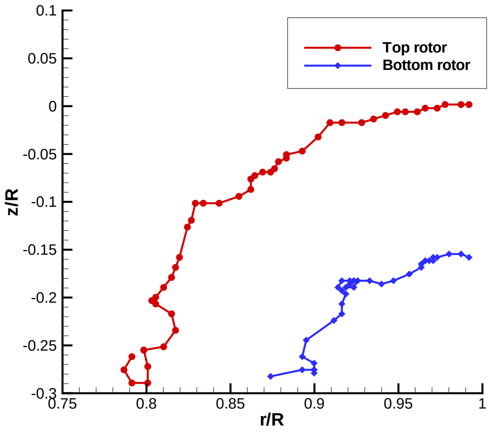

(c) r/R vs z/R

Figure 16: Wake trajectory for the coaxial system (case 7) when the blades are aligned.

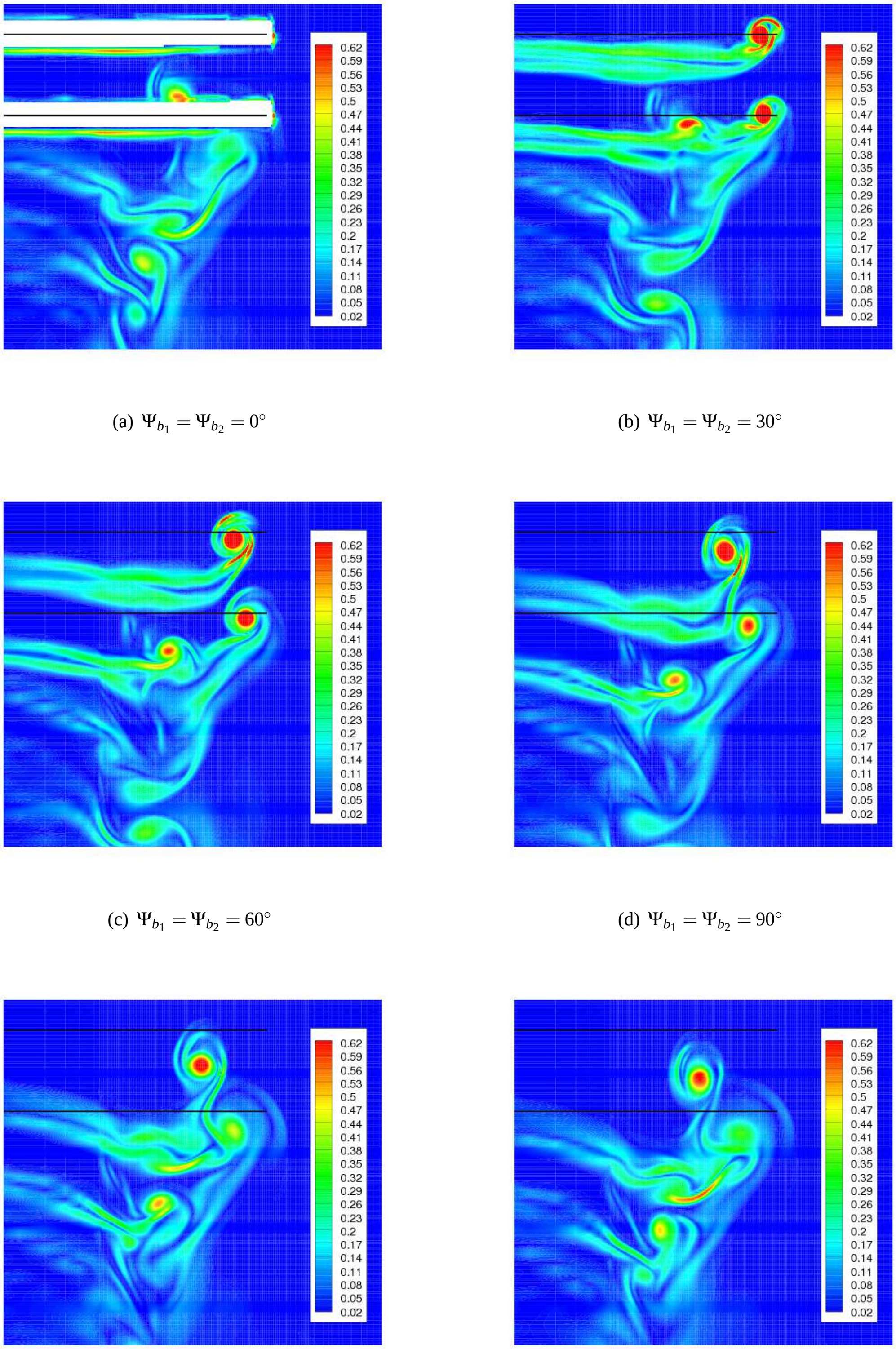

(a) $\Psi_{b_1} = \Psi_{b_2} = 0^\circ$

(b) $\Psi_{b_1} = \Psi_{b_2} = 30^\circ$

(c) $\Psi_{b_1} = \Psi_{b_2} = 60^\circ$

(d) $\Psi_{b_1} = \Psi_{b_2} = 90^\circ$

(e) $\Psi_{b_1} = \Psi_{b_2} = 120^\circ$

(f) $\Psi_{b_1} = \Psi_{b_2} = 150^\circ$

Figure 17: Vorticity magnitude contours in a fixed plane in space for the coaxial system at different instances in time (case 7).

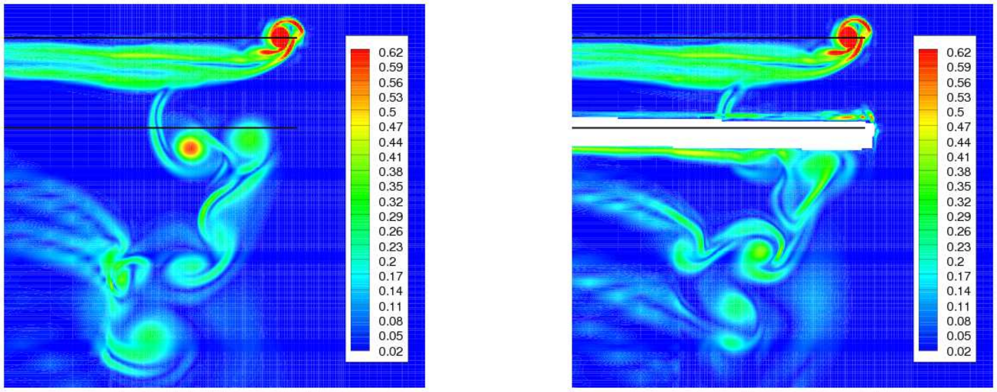

(a) $\Psi_{b_1} = 30^\circ$, $\Psi_{b_2} = 150^\circ$

(b) $\Psi_{b_1} = 30^\circ$, $\Psi_{b_2} = 0^\circ$

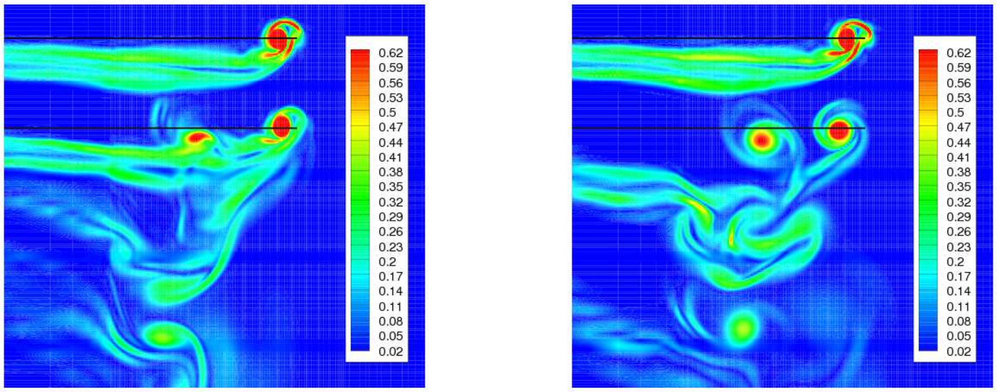

(c) $\Psi_{b_1} = 30^\circ$, $\Psi_{b_2} = 30^\circ$

(d) $\Psi_{b_1} = 30^\circ$, $\Psi_{b_2} = 60^\circ$

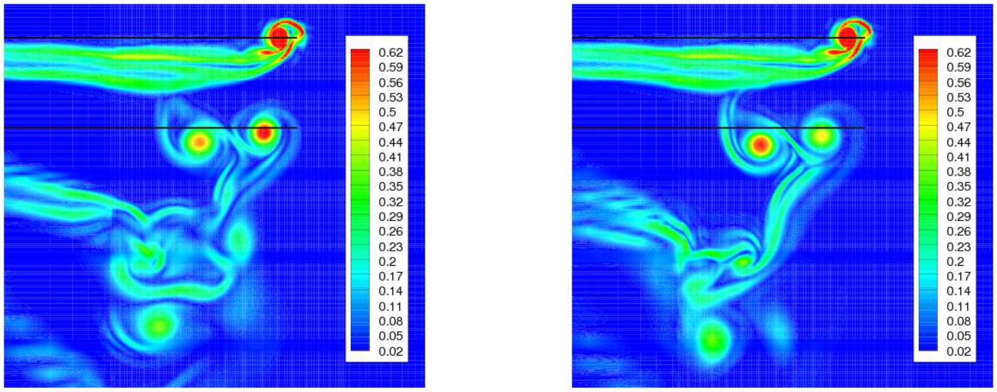

(e) $\Psi_{b_1} = 30^\circ$, $\Psi_{b_2} = 90^\circ$

(f) $\Psi_{b_1} = 30^\circ$, $\Psi_{b_2} = 120^\circ$

Figure 18: Vorticity magnitude contours in a plane that is at 30° azimuth from the top rotor blade at different instances in time (case 7).

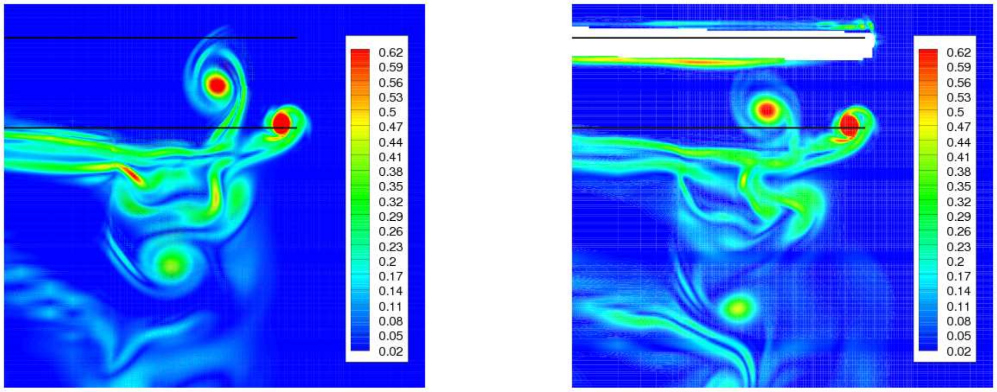

(a) $\Psi_{b_1} = 150^\circ, \Psi_{b_2} = 30^\circ$

(b) $\Psi_{b_1} = 0^\circ, \Psi_{b_2} = 30^\circ$

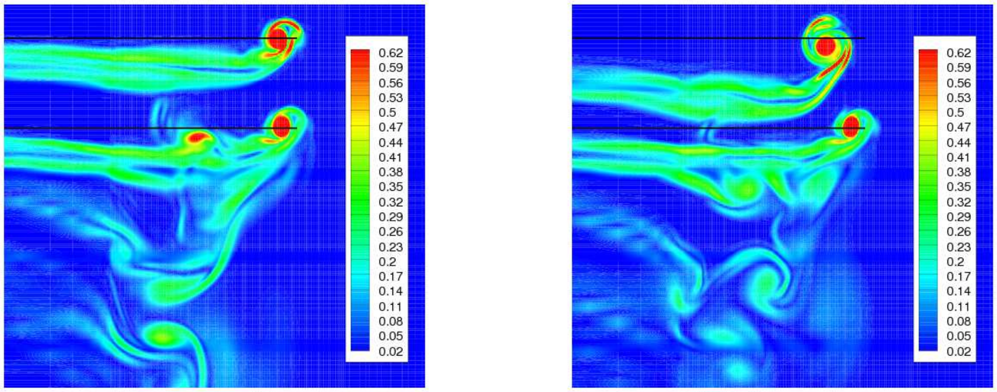

(c) $\Psi_{b_1} = 30^\circ, \Psi_{b_2} = 30^\circ$

(d) $\Psi_{b_1} = 60^\circ, \Psi_{b_2} = 30^\circ$

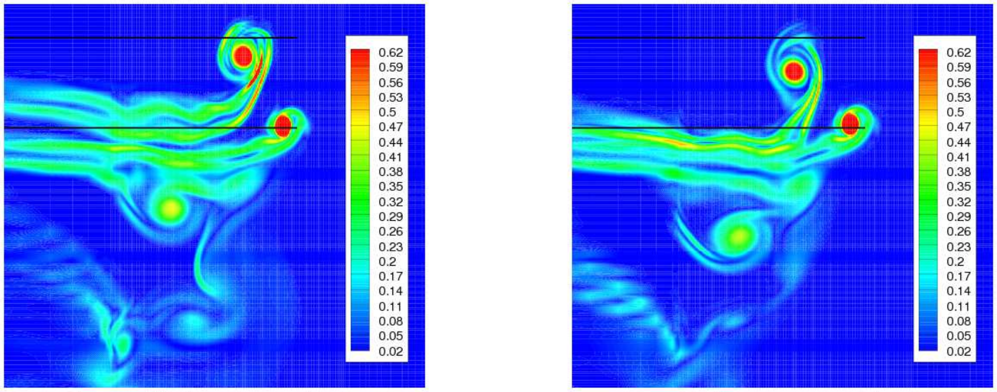

(e) $\Psi_{b_1} = 90^\circ, \Psi_{b_2} = 30^\circ$

(f) $\Psi_{b_1} = 120^\circ, \Psi_{b_2} = 30^\circ$

Figure 19: Vorticity magnitude contours in a plane that is at 30° azimuth from the bottom rotor blade at different instances in time (case 7).

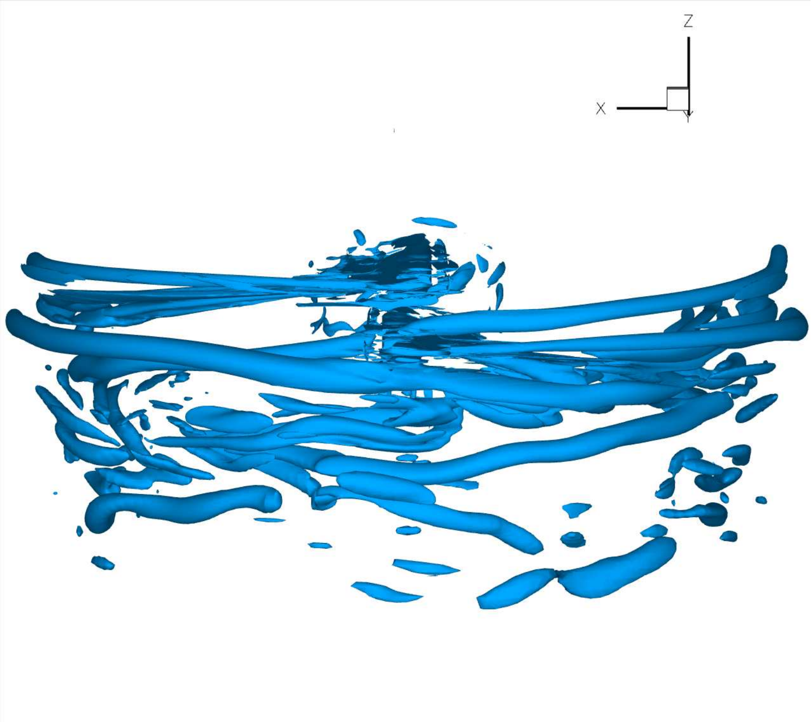

(a) Vortex structures

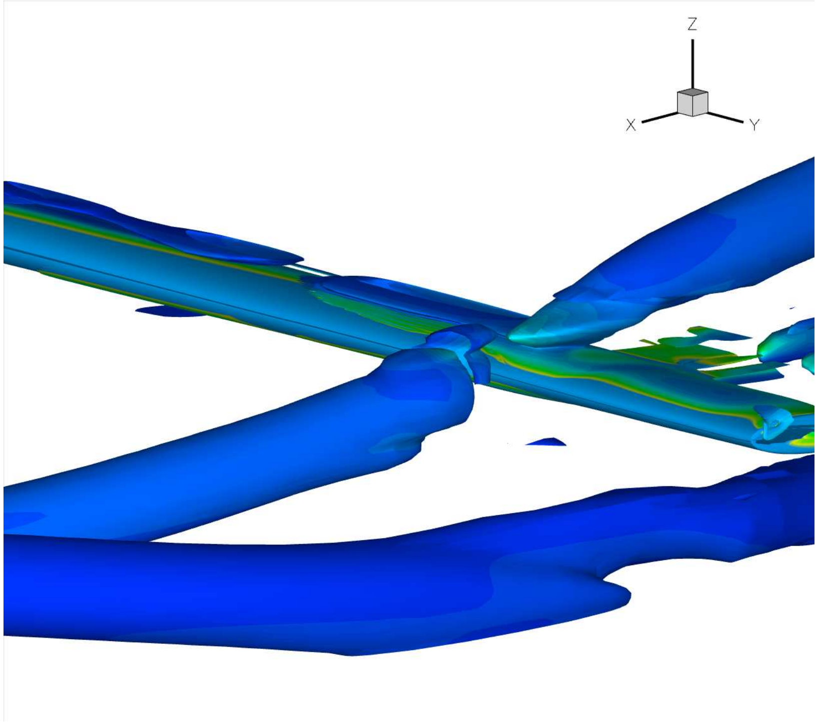

(b) Tip vortex from top rotor interacting with bottom rotor

Figure 20: Iso-surfaces of the second invariant of vorticity magnitude ($q = 0.1$) for the coaxial system (case 7).